Journal Pre-proof

In-situ Formation of mesoporous SnO$_2$@C Nanocomposite Electrode for Supercapacitors

Malothu Usha Rani , Vangapally Naresh , Devarakonda Damodar , Sadananda Muduli , Surendra Kumar Martha , Atul Suresh Deshpande

Please cite this article as: Malothu Usha Rani , Vangapally Naresh , Devarakonda Damodar , Sadananda Muduli , Surendra Kumar Martha , Atul Suresh Deshpande , In-situ Formation of mesoporous SnO$_2$@C Nanocomposite Electrode for Supercapacitors, *Electrochimica Acta* (2020), doi: https://doi.org/10.1016/j.electacta.2020.137284

This is a PDF file of an article that has undergone enhancements after acceptance, such as the addition of a cover page and metadata, and formatting for readability, but it is not yet the definitive version of record. This version will undergo additional copyediting, typesetting and review before it is published in its final form, but we are providing this version to give early visibility of the article. Please note that, during the production process, errors may be discovered which could affect the content, and all legal disclaimers that apply to the journal pertain.

HIGHLIGHTS

- One-pot synthesis of mesoporous SnO_2@C composite is achieved using polymer beads

- Interconnected porous structure allows full accessibility of electrolyte ions to SnO_2

- It exhibits high specific capacitance of 368 F g^{-1} at 1 Ag^{-1} in aqueous electrolyte

- Achieved high energy density of 24.5 Wh kg^{-1} and power density of 346 W kg^{-1}

- 95.5 % of initial capacitance retained after 2000 cycles at 2 A g^{-1} current density

In-situ Formation of mesoporous SnO$_2$@C Nanocomposite Electrode for Supercapacitors

Malothu Usha Rani[a], Vangapally Naresh[b], Devarakonda Damodar[a], Sadananda Muduli[b], Surendra Kumar Martha[b,*] and Atul Suresh Deshpande[a,**]

[a]Department of Materials Science and Metallurgical Engineering, Indian Institute of Technology Hyderabad, Kandi, Sangareddy, 502285, Telangana, India

[b]Department of Chemistry, Indian Institute of Technology Hyderabad, Kandi, Sangareddy, 502285, Telangana, India
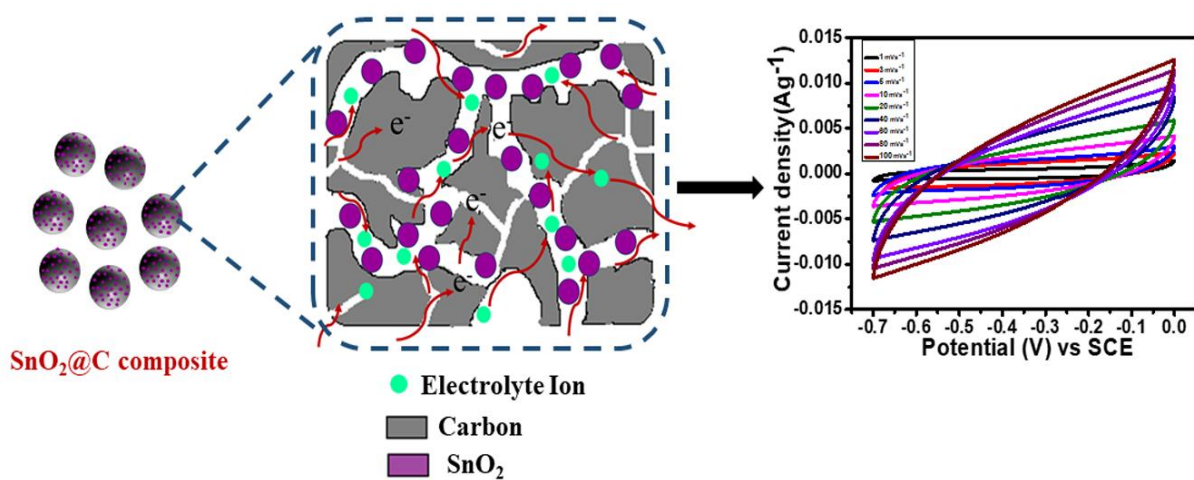
*Corresponding author

Email address: martha@chy.iith.ac.in (S.K.Martha)

** Corresponding author.

Email address: atuldeshpande@msme.iith.ac.in (A.S.Deshpande).

Graphical abstract

SnO₂@C composite

● Electrolyte Ion

Carbon

SnO₂

ABSTRACT

In this work, we report a supercapacitor based on SnO_2@C composite electrode with better electrochemical performance. SnO_2@C composite is synthesized from porous polymer beads by the impregnation method. The resultant composite is porous and retains uniform spherical morphology of polymer beads. The composite exhibits the bimodal distribution of pores with a specific surface area of 286 $m^2 g^{-1}$. SnO_2@C composite electrode show specific capacitance of 432 F g^{-1} at 1 A g^{-1} in 1M KOH electrolyte with capacitance retention of 95.5% for 2000 cycles. Besides, the composite electrode shows an energy density of 29.4 Wh kg^{-1} at a power density of 418 W kg^{-1} at 1 A g^{-1} current density. The optimize electrode design improves cyclic stability due to reducing crystal growth of SnO_2 as well as diffusion kinetics because of the presence of bimodal pores which provides continuous electron path. The bimodal micropores and mesopores in carbon matrix have the accessibility of electrolyte to SnO_2, improving overall electrochemical performance and therefore SnO_2@C composite is suitable as electrode material for supercapacitors.

1. Introduction

The superior properties of carbon-based materials such as high specific surface area, chemical stability, good electrical conductivity, tunable pore size *etc.* have made them the most widely used electrode materials for supercapacitors [1]. Among the various carbon materials such as activated carbon [2], carbon nanofibers [3], graphene [4], carbon nanotubes [5] etc. mesoporous carbon plays a significant role in improving the electrochemical performance of supercapacitors due to their mesoporous structure. The mesopores facilitate the rapid ion transportation at the electrode-electrolyte interface [6]. There are different ways of synthesizing mesoporous carbons such as sol-gel process [7], template-based method [8], and carbonization followed by activation of carbon precursors containing pore-forming agent [9]. Evolution of carbon with controllable pore structure is complex in the case of sol-gel and carbonization processes [10]. Synthesizing mesoporous carbon with controlled pore structure is possible using templating technique. Hard templates such as SAB-15, MCM-48 (ordered mesoporous silica molecular sieves) are generally used to synthesize mesoporous carbon [11]. Apart from mesopores, micropores also contribute significantly towards the formation of an electrical double layer due to the high specific surface area of the electrode [12]. Therefore, the presence of both mesopores (for rapid ion transport) and micropores (for charge accumulation) with interconnected nature are necessary for improving the electrochemical performance of the carbon electrode. The interconnected porosity helps in providing a continuous path for ion transport.

Although the carbon-based materials are widely used electrode materials for supercapacitors, their use is restricted in certain applications due to its low specific capacitance and energy density. The specific capacitance of carbon can be improved by combining it with pseudocapacitive metal oxides such as RuO_2, MnO_2, NiO, Co_3O_4, Fe_2O_3

and SnO_2 [13]. Among the well-known metal oxides, SnO_2 has gained more attention due to its n-type semiconductor nature (having wide energy gap ($Eg = 3.62$ eV, at 300 K)), high specific capacitance, low cost and non-toxic. It can be used in a wide range of electrolytes such as an acidic, neutral and aqueous electrolyte [14]. SnO_2 is widely used electrode material for supercapacitor application due to its low electron chemical potential which results in fast redox and high chemical stability [15]. There are several reports on C-SnO_2 composite materials which exhibited excellent electrochemical performance. Ordered mesoporous carbon and SnO_2 composite showed a specific capacitance of 200 F g^{-1} at 5 mV s^{-1} and stable over 500 cycles due to confinement of nanosized SnO_2 in the mesoporous carbon and shorter diffusion path provided by mesoporous carbon [16]. The direct channels for electron transport provided by SnO_2 nanoflowers in SnO_2-graphene composite show a specific capacitance of 126 F g^{-1} at 0.2 A g^{-1} current density and stable over 2000 cycles [17]. SnO_2 nanoparticles anchored on graphene composite synthesized via chemical reduction method with a specific surface area of 241.32 m^2g^{-1} retains 95% of initial capacitance (205 F g^{-1}) after 1000 cycles at 10 mA g^{-1} [18]. The excellent performance of the composite is due to the spacer effect of the SnO_2 nanoparticles and electrical double layer capacitance from graphene. The morphology of SnO_2 dots on uniformly anchored over activated porous carbon nanofibers processed through hard templating method showed a high specific capacitance of 225.4 F g^{-1} at 1 A g^{-1} current density [19]. A report on 2D SnO_2 nanoplatelets decorated on graphene (Surface area 560 m^2g^{-1}) displayed high specific capacitance of 294 F g^{-1} at 2 A g^{-1} with 100 % capacitance retention for first 200 cycles and 90 % after 2000 cycles due to increase in the surface to the surface contact area between graphene and SnO_2 nanoplatelets which improved the diffusion kinetics [20]. SnO_2/CNFs composite was fabricated by electrospinning followed by solvothermal method. Due to high-level exposure of SnO_2 nanoparticles on the surface of the composite, a specific capacitance of 187 F g^{-1} at 20 mV s^{-1}

was observed [21]. A composite of functionalised carbon cloth @ SnO_2 showed a specific capacitance of 197 F g^{-1} at 1 A g^{-1}. Carbon cloth acts as conductive channels for the fast transfer of electrons and ions and SnO_2 nanoclusters facilitate the charge storage [22]. Core shell SnO_2/SWCNTs synthesized by electrodeposition method exhibited a specific capacitance of 320 F g^{-1} at 6 mV s^{-1}. The SWCNTs in the core-shell nanowires provides the electronic conductive channels due to the excellent conductivity of SWCNTs [23]. The composite rGO/SnO_2 synthesized via chemical route showed 348 F g^{-1} at 50 mA g^{-1}. SnO_2 acts as spacer between the graphene layers as well as maximizes the hydrophilic nature which improves electrochemical performance [24]. Hydrothermally synthesized flower-like SnO_2/graphene [25] exhibited 396 F g^{-1} at 4.5 A g^{-1}, with a capacitance retention of 92.6% even after 10 000 cycles. The specific surface area and morphology of SnO_2 in the composite also affect the electrochemical performance.

In this study, we report SnO_2@C composite synthesized using commercial porous polymer beads by one pot, scalable and simple impregnation method. The polymer beads act as a template as well as a carbon precursor. The advantage of using these polymer beads is, they have a high specific surface area, interconnected porosity and well-defined pore size [26]. The small pore size of polymer beads can prevent rapid crystal growth of SnO_2 which increases the specific surface area of the electrode. The high specific surface area can accumulate more electrolyte ions at the electrode-electrolyte interface which leads to higher specific capacitance. There is an in-situ evolution of carbon and SnO_2 during carbonization which leads to a strong interaction between carbon and SnO_2 and may further help in rapid electron transfer throughout the whole electrode. It can further improve cyclic stability and C rate performance.

2. Experimental

2.1. Synthesis of SnO$_2$@C composite

SnO$_2$@C composite was synthesized by the impregnation method. Amberlite XAD-16N (Alfa Aesar), porous polymeric beads of polystyrene were used as carbon precursor. These porous beads were chosen because they are designed to use in size exclusion chromatography having interconnected pores with an average pore diameter of ~10 nm and high surface area. Before the synthesis of SnO$_2$@C composite, these porous polystyrene beads were washed repeatedly with DI water to remove salts such as NaCl and Na$_2$CO$_3$. 1 g of wet amberlite XAD-16N beads were added to 1.4 g (0.0062 moles) of SnCl$_2$.2H$_2$O (Alfa Aesar) dissolved in 5 ml of absolute ethanol. The suspension was then sonicated for 15-20 min using bath sonicator to ensure infiltration of metal chloride solution into the porous beads. After sonication, the suspension was agitated 24 h to allow sufficient time for impregnation. The impregnated beads were then dried in a hot air oven at 60 °C for 24 h. The drying step allows the tin precursor to infiltrate and fill the pores within polymer beads by capillary action. Accordingly, the amount of SnCl$_2$ needed to fill the pores was calculated based on the pore volume of the polymer beads specified by the supplier. The dried impregnated beads were carbonized at 700 °C for 1 h with a heating rate of 5 °C min^{-1} under argon atmosphere using tubular furnace (Sigma Scientific Instruments Pvt. Ltd, Chennai, India) to form porous SnO$_2$@C composite. During carbonization, the polymer converts into carbon and impregnated SnCl$_2$.2H$_2$O converts into SnO$_2$ yielding a porous SnO$_2$@C composite. For comparison, we have washed the polymer beads repeatedly with DI water and dried in a hot air oven at 60 °C for 24 h. The dried polymer beads are directly carbonized at 650 °C, 700 °C, 800 °C without infiltrating the tin precursor under argon atmosphere are denoted as C-650 °C, C-700 °C and C-800 °C. For the comparison electrochemical performance C-700 °C sample was used and is denoted as the reference carbon.

2.2. Structural and physical characterizations

The crystallinity of $SnO_2@C$ composite was studied using XRD (X-ray diffractometer) and Raman spectroscopy. XRD pattern was acquired using Rigaku ultima IV X-ray diffractometer, equipped with Cu–k_α radiation (wavelength, λ= 1.54 Å) source. Bruker (SENTERRA) micro Raman spectrometer with the excitation laser source of wavelength 532 nm was used to record the Raman spectra. Morphological analyses were carried out using field emission scanning electron microscope (FE-SEM) (JEOL JSM-7800F) and transmission electron microscope (TEM) (JEOL JEM 2100). Nitrogen sorption studies (BET analysis) of carbonized samples were performed using Quantachome ASiQwin^{TM} instrument. The sample was degassed at 300 °C for 4 h before the BET analysis. Thermal degradation behaviour of $SnO_2@C$ samples was assessed by using SDT Q600 TGA analyser (TA instruments). Thermogravimetric analysis (TGA) of the sample was carried out till 900 °C in air. The surface analysis of elements was analysed by elemental mapping and X-ray photoelectron spectroscopy (XPS). XPS measurements were carried out using ESCA+, (Omicron nanotechnology, Oxford Instruments Plc., Germany) equipped with monochromic AlKα (1486.6 eV) X-ray beam radiation operated at 15 kV and 20 mA, binding energy was calibrated vs. carbon (C1s = 284.6 eV). XPS data were deconvoluted using Origin 8.0 software.

2.3. Electrochemical characterizations

The capacitive behaviour of carbon and $SnO_2@C$ beads was carried out by using cyclic voltammetry (CV), galvanostatic charge-discharge (GCD) measurements and electrochemical impedance spectroscopic studies (EIS) in a three-electrode setup using 1M KOH electrolyte. At 25°C, 1 M KOH shows specific conductivity of 0.2153 S cm^{-1}. KOH in the aqueous medium has the sizes of 3.31 Å (K$^+$) and 3.0 Å (OH$^-$). K$^+$ has the highest ionic conductivity after H_3O^+ among cations and OH$^-$ has the highest ionic conductivity among

anions. The platinum sheet used as a counter electrode, C-SnO$_2$ or reference carbon coated on to graphite sheet used as working electrode, and Hg/Hg$_2$Cl$_2$ acts as a reference electrode. In this experiment graphite sheet (Graphite India) used as a current collector for the working electrode. The area of the working electrode was 4 cm^2 (2 cm × 2 cm) with active material loading is about 0.9 mg cm$^{-2.}$ The working electrode was prepared by using 80 % of Carbon/SnO$_2$@C or reference carbon calcined at 700 ^{o}C as active material, 10 % of carbon black (Super P, C65) conductive additive and 10 % of Polyvinylidene fluoride (PVDF) (Kureha KF Polymer 9300 PVDF) binder in dimethylformamide (DMF) (Sigma-Aldrich) solution. These materials were ball milled together to form a thick slurry which is coated onto the graphite sheet using a doctor blade, followed by drying at 100 ^{o}C for 12 h under vacuum. The CV and GCD performances were measured in potential range in between -0.7 to 0 V. All the electrochemical experiments were characterized by using a cell test system (Solartron analytical, Oak Ridge, TN, USA) model 1470E coupled with an FRA model 1455A. The EIS responses were recorded under the fully discharged condition within the frequency range of 1 MHz and 10 mHz at an amplitude of 5 mV. Further, the obtained EIS data were analysed using Z-view software (Scribner Associates, USA).

3. Results and discussions

3.1. Structural and physical characterizations

The synthesis of SnO$_2$@C composite from porous polymer beads precursor is illustrated in scheme 1. The phase identification of SnO$_2$@C composite shown in the XRD pattern in Fig. 1a confirms the tetragonal rutile phase of SnO$_2$ (JCPDS number 41-1445) [27]. The diffraction peaks of carbon are not distinguishable in XRD pattern which indicates that carbon may be poorly crystalline or glassy. The average crystallite size of SnO$_2$@C calculated from FWHM value of (110) peak using the Scherrer equation was found to be 16

nm. The Raman spectrum (Fig. 1b) of SnO_2@C composite shows Raman bands around 467 cm^{-1} and 622 cm^{-1} which can be attributed to the E_g and A_{1g} modes of the SnO_2 phase [28] [29] [30]. Among E_g and A_{1g} modes, A_{1g} mode is seen prominently. Additionally, bands at 1590 cm^{-1} and 1330 cm^{-1} which are typical for sp^2 carbons are also observed [31]. The 1590 cm^{-1} band corresponds first-order scattering of the E_{2g} symmetry of sp^2 bonded carbon atoms in a 2-dimensional hexagonal lattice (G-band) [32]. Whereas, the D-band at 1330 cm^{-1} is characteristic of defects or disorderness in the sample, corresponding to breathing mode with A_{1g} symmetry [33].

The Supplementary Fig. S1 shows Raman spectra of SnO_2@C composite and carbon without SnO_2. The I_D/I_G ratio of carbon without SnO_2 is 1.60 in relation to SnO_2@C composite of 2.45, indicating an increase in the disorderness due to SnO_2 incorporation. The I_D/I_G ratio indicates that carbon exists in a predominantly glassy form [34]. Thermogravimetric analysis (TGA) was performed to determine the content of tin oxide in the SnO_2@C composite (Fig. 1c). A small weight loss of 3.9 wt. % till 150 °C is attributed to the removal of moisture from the sample, and significant weight loss from 375 °C to 665 °C corresponds to the decomposition of carbon in the presence of air. After 665 °C, temperature stable up to 900 °C indicates no weight loss in the sample. 50 wt. %. of SnO_2 and 46.1 wt. % of carbon is calculated from the TGA graph.

The porous structure and specific surface area (SSA) of SnO_2@C composite are determined by using Brunauer-Emmett-Teller (BET) method shown in Fig. 1d. The isotherm of commercial polymer beads used in this synthesis shows typical type-IV isotherm which is a characteristic of a mesoporous sample with an SSA of 753 m^2/g (Supplementary Fig. S2 (a)). The pore size distribution evaluated from Barrett-Joyner-Halenda (BJH) method) is shown in Supplementary Fig. S2 (b) which indicates a maximum number of pores with pore size in the range of 10-12 nm. Similar to polymer beads, the SnO_2@C composite also shows

Type-IV isotherm with an SSA of 286 m^2g^{-1} and micropore surface area of 167 m^2g^{-1} (Fig. 1d and Fig. S2(c)). Fig. 1d inset and Fig.S2(d) shows that the pore size distribution from the BJH method exhibits a bimodal distribution of pores with pore sizes of 1.8 nm and 10 nm, i.e. a combination of mesopores and micropores. The details of SSA and pore characteristics of polymer beads and SnO_2@C composite are summarized in Table. 1. The decomposition of the polymer during the carbonization process may be responsible for the presence of micropores in the SnO_2@C composite. The presence of mesopores facilitate rapid ion transport and act as ion reservoirs of electrolyte and consequently reduce the diffusion distances of ions to the carbon surface, ensure high rate capability and high power density [35]. The micropores exhibit high capability for charge accumulation at the electrode-electrolyte interface. There is a slight decrease in the pore size and increase in the microporosity. The polymer beads are infiltrated with $SnCl_2.2H_2O$ which decomposes during carbonization and creates porosity which is evident from the high magnification TEM image (Fig.3b). To understand the role of presence of tin precursor on porosity and surface area of carbonized sample, polymer beads without infiltration with $SnCl_2$ were carbonized at different temperatures. The detailed pore analysis of polymer beads and reference carbon beads are mentioned in Table.S1 and Fig.S2 (e) and (f). Supplementary Fig.S2 (e) and (f) show the BET isotherms and pore size distribution of beads carbonized at 650 °C, 700 °C and 800 °C without $SnCl_2$ infiltration. The SSA of C-650 °C, °C, C-700 °C and C-800 °C samples were found to be 304 m^2g^-1, 317 m^2g^{-1} and 342 m^2g^{-1} respectively, which are less than the SSA of polymer beads. Furthermore, the isotherms of carbonized beads shown in the Supplementary Fig. S2 (e)) are non-identical with that of polymer beads. The pore size distribution from the BJH method (shown in Supplementary Fig. S2 (f)) exhibits a maximum number of pores with a pore size of 1.9 nm, indicating the majority of micropores. The increase in the micropores is due to the shrinkage of the pore size after heat treatment. The

beads carbonized at 800 °C shows high SSA compared to beads carbonized at 650 °C. This may be due to the partial decomposition of polymer beads at 650 °C. It is evident from these results that carbonization of polymer beads without infiltration with the tin precursor leads to collapse of pore structure of the polymer beads which results in loss of pore geometry and specific surface area.

Table 1. Comparison of porous characteristics of polymer beads and $SnO_2@C$ composite.

Sample	Isotherm	S_{BET} (m^2 g^{-1})	S_{micro} (m^2 g^{-1})	V_t (cm^3 g^{-1})	V_{mic} (cm^3 g^{-1})	V_{meso} (cm^3 g^{-1})	V_{micro}/V_t (%)	V_{meso}/V_t (%)
Polymer beads	Type-1V	753	85	1.56	0.031	1.52	2	98
$SnO_2@C$	Type-1V	286	167	0.35	0.087	0.26	25	75

S_{BET}: Specific surface area by the BET method, S_{micro}: Micropore surface area evaluated by t-plot method, V_t: Total pore volume, V_{mic}: Micropore volume, V_{meso}: Mesopore volume.

The spherical morphology of the polymer beads is shown in Fig.S3(a). The porous nature of the polymer beads is observed at high magnification image (Fig.S3(b)). Fig.S3(c) shows the morphology of the beads carbonized at 650 °C. The particle size of the beads decreases after carbonization due to shrinkage. Fig.S3(d) depicts a higher magnification image of carbonized beads which do not show clear porosity due to collapse of pore structure after heat treatment. The morphology of $SnO_2@C$ composite shown in the SEM image of Fig. 2 a-b and Fig.S3(e)reveals that even after carbonization of polymer beads, $SnO_2@C$ composite still retains the spherical morphology of the precursor beads with smooth exterior surface

indicating the absence of excess SnO_2 deposition on the surface. The elemental distribution using energy dispersive spectroscopy (EDS) analysis (Supplementary Fig. S4) shows even distribution of Sn, O and C on the surface of SnO_2@C beads. During sample preparation, some of the beads were intentionally broken to observe the distribution of SnO_2 in the interior parts of the beads as well as to assess if any uneven shrinkage occurred during carbonization. Fig. 2c shows the low-magnification image of broken beads which shows even morphology devoid of any cracks. Higher magnification images of the broken part of SnO_2@C beads (Fig. 2d and S3(f)) reveal granular morphology with homogenous porosity indicating that carbonization does not lead to uneven shrinkage or cracks. The morphology of SnO_2@C composite is further characterized by TEM as shown in Fig. 3. It shows that SnO_2 nanoparticles are evenly distributed in the porous carbon indicating homogenous impregnation of Sn precursor during synthesis (Fig.3a) As shown in the inset to Fig. 3a, the average particle diameter of these SnO_2 nanoparticles based on 100 measurements was found to be 7.1 ± 2.8 nm. The size of the SnO_2 nanoparticles is within the pore size of the precursor polymer beads (10-12 nm) indicating a restricted crystal growth of SnO_2 nanoparticles. Some of the SnO_2 particles may coalesce and form elongated rod like particle and can be trapped inside the pore of the bead which is shown in supplementary Fig.S5. The circled regions indicate coalesce of two particles and representing as a single elongated particle. The elongated particle shows two crystallites having lattice fringes oriented in the same direction. The d-spacing of the two crystallites corresponds to (110) reflection of SnO_2. The coalesce elongated particle size is found to be 14 nm which might be the reason for higher crystallite size of SnO_2 obtained from the XRD.

The infiltration of tin precursor in the beads creates porosity which is shown in Fig.3b. Further, the in-situ evolution of carbon and SnO_2 from their precursors during carbonization leads to the strong interaction of SnO_2 with the carbon and may help in rapid

electron transfer throughout the whole electrode. Fig. 3c displays high magnification image of individual SnO_2 nanoparticle with well-defined lattice fringes indicating that these particles are well-crystallized. The interlayer spacing between the lattice fringes of SnO_2 is about 0.334 nm (inset of Fig. 3c) which corresponds to the d-spacing between (110) planes of the SnO_2 and is consistent with the d-spacing of SnO_2 calculated from XRD. Fig. 3c shows that carbon consists of nano graphitic domains. The interlayer spacing between the lattice fringes of carbon layers is 0.35 nm indicating the disordered structure of the carbon which supports the findings from Raman studies. The selected area electron diffraction (SAED) pattern of SnO_2 (Fig. 3d) shows a well-resolved set of concentric rings, corresponding to (110), (101) and (211) planes of SnO_2. The bonding and the oxidation state of elements in SnO_2@C composite were analyzed by XPS as shown in Fig. 4. The survey spectrum of Fig. 4a confirms the presence of C, O and Sn elements [14]. The core-level spectrum of Sn3d (Fig. 4b) exhibits two peaks: the main peak ($3d_{5/2}$) and a satellite peak ($3d_{3/2}$) with binding energies of 487.59 eV and 496.09 eV, respectively which are assigned to +4 oxidation state of Sn. There are no peaks of other chemical oxidation states of Sn indicating the presence of Sn^{4+} in the composite. The peak distance between $Sn3d_{5/2}$ and $Sn3d_{3/2}$ is 8.5 eV. The peak position and peak distance are identical to the binding energies reported for SnO_2 [36]. The deconvoluted C 1s spectrum of Fig. 4c consists of six peaks: peaks at a binding energy of 283.2 eV, 284.6 eV, 285.9 eV, 287.4 eV, 288.9 and 291.83 eV corresponds to sp^2 binding energy peak of C-C molecular bond , C- C (sp^2 bonded), C-C, C=O, O-C=O and π-π^* respectively [37–39]. The deconvoluted O 1s spectrum (Fig. 4d) consists of three peaks centred at binding energies of 531.5 eV, 532.5 eV and 533.5 eV, corresponding to O-Sn/C=O, C-O-Sn/C-O-C/C-OH, and O-C=O functional groups, respectively [19, 21].

*3.2. Electrochemical performance studies*

The polymer beads after carbonization undergo structural collapse and result in loss of SSA. Therefore, the electrochemical characteristics of reference carbon and $SnO_2@C$ composite are performed using the aqueous three-electrode system. Electrochemical performances as CV and charge-discharge studies of reference carbon sample as shown in Supplementary Fig. S6. The CV curves deviate from rectangular behaviour (Supplementary Fig. S6a) at high scan rates. At low scan rates of 1 mV s^{-1} (Supplementary Fig. S6b), the CVs are quasi-rectangular in shape. The deviation at a high scan rate is due to kinetics limitations, as electrolyte ions are not accessed at the interior of the active material. $SnO_2@C$ capacitive behaviour was studied in the potential range between -0.7 to 0 V in 1 M aqueous KOH electrolyte solution. CVs at scan rates of 1, 5, 10, 20, 40, 60, 80 and 100 mV s^{-1} of $SnO_2@C$ composite electrode is shown in Fig. 5a. The CV curves are not perfectly rectangular (Fig. 5a) indicates both electric double-layer capacitors (EDLC) due to carbon and Pseudocapacitive behaviour due to SnO_2. At low scan rates of 1 mV s^{-1} (Fig. 5b), the CVs are quasi-rectangular in shape and as the scan rate increases deviation from the rectangular shape is observed. The deviation at high scan rate is due to kinetics limitations, as electrolyte ions are not accessed at the interior of the active material. CV curves at various scan rates do not exhibit the redox peaks because of more utilization of the active material and therefore it is charged and discharged completely. Redox behaviour depends on insertion-de insertion of ions from the electrolyte.

The specific capacitance of $SnO_2@C$ composite is investigated from the charge-discharge profiles. The charge-discharge profiles are asymmetric and time duration is long in comparison to normal EDLC as it exhibits typical pseudo capacitive property. The specific capacitance of the $SnO_2@C$ composite is calculated by the following formula [40].

$$C_{sp} = \frac{2I\int Adt}{V^2}$$

Where C_{sp} is the specific capacitance, I is current density, $\int Adt$ is the integral area, V is discharge voltage range excluding voltage (IR) drop.

SnO$_2$@C galvanostatic charge-discharge profiles measured at various current densities (shown in the Fig. 5c) shows specific capacitance of 432, 343, 326, 306 and 280 F g^{-1} at current densities of 1,2,3,5 and 10 A g^{-1}, respectively, which is superior to many SnO$_2$@C composites reported in the literature (shown in Table.2). As the current density increases specific capacitance decreases due to electrolyte containing positive ions (K$^+$) approach the only outer surface of the electrode (characteristic of redox behaviour), whereas at low scan rates positive ions (K$^+$) will easily enter to the interior of the electrode which leads to higher specific capacitance. In basic (KOH) medium, Pseudo capacitive origin comes from the K$^+$ ion of the electrolyte solution electrochemically adsorbed onto the surface of the SnO$_2$. The surface of the SnO$_2$ particles was adsorbed and desorbed as per the following equation.

$$(SnO_2)_{surface} + K^+ + e^- \longleftrightarrow (SnO_2^- - K^+)_{surface} \qquad (2)$$
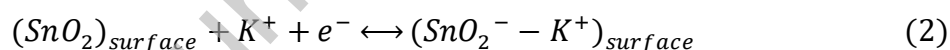
The specific capacitance of pure SnO$_2$ (in KOH electrolyte) reported in the literature is shown in supplementary Table.S2. Based on the literature reports pure SnO$_2$ influences around 30-50 % the total capacitance of the composite. Adsorption and desorption processes possess charge–storage property signifies an improvement in the kinetics of the composite electrode. Charge –discharge profiles (Fig. 5c) having a sudden voltage drop observed during the initial stages of the discharge cycle is due to IR drop (internal resistance) of the electrode. As current density increases voltage drop increases and decreases the specific capacitance. The electrochemical performances of beads carbonized at 700 ^{o}C (reference carbon) were carried

similar to $SnO_2@C$. The electrochemical performance such as cyclic voltammetry (CV) and galvanostatic charge-discharge curves are shown in Supplementary Fig. S6. Supplementary Fig. S6c shows the carbon sample measured at 1 and 2 A g^{-1} delivers specific capacitances of 35 and 3 F g^{-1}, respectively, Further, at higher currents, no capacitance is observed. This could be due to more voltage drop ((IR) detected during the discharge. A comparison of specific capacitances of $SnO_2@C$ and Carbon samples in Supplementary Figure S6d shows specific capacitance of 432 and 35 F g^{-1} at 1 A g^{-1}. In as-synthesized $SnO_2@C$ composite, in-situ evolution of carbon and SnO_2 from their precursors during carbonization leads to the strong interaction of SnO_2 with the carbon and helps in rapid electron transfer throughout the electrode. Subsequently, it helps to increase the specific capacitance of the material. Moreover, Polymer beads after carbonization undergo decomposition which results in the structural collapse, which results in very less specific capacitance in reference carbon. In overall, the contribution of carbon in $SnO_2@C$ composite is very low. Comparison of the specific capacitance of the reference Carbon and $SnO_2@C$ composite calculated from the CV curves is shown in supplementary figure S7.

C-rate performances of $SnO_2@C$ composite electrode shown in Fig. 5d demonstrates that after cycling high current densities (5 and 10 A g^{-1}) when back to a low current density of charge-discharge studies, the electrodes exhibit good capacity retention indicating good stability of these electrodes at low and high rates.

Table 2. Comparison of Electrochemical characteristics of $SnO_2@C$ composite.

Composite	Synthesis Method	Scan rate / Current density	Electrolyte	Specific capacitance ($F\ g^{-1}$)	Capacitance retention (%)	References
$SnO_2@C$	chemical	5 mV s^{-1}	1M H_2SO_4	37.8	-	[41]
$SnO_2@carbon$ aerogel	Sol-gel method	10 mA g^{-1}	1M H_2SO_4	69.8		[42]
$SnO_2@CNF$	Electrospinning	1 A g^{-1}	1M H_2SO_4	118	94.6 % after 10000 cycles	[43]
SnO_2 @Graphene	Chemical	0.2 A g^{-1}	1M H_2SO_4	126	98.2% after 2000cycles	[17]
SnO2@MWCNT	Sonochemical	1 A g^{-1}	4.5 M H_2SO_4	133.33	-	[44]
$C@SnO_2$	Chemical	2 A g^{-1}	4.5 M H_2SO_4	150	>90% after 1000 cycles	[45]
SnO_2 @Graphene	Chemical	1 A g^{-1}	6 M KOH	184	-	[46]
FCC@ SnO_2	solvothermal	1 A g^{-1}	1 M Na_2SO_4	197.7	95.5% after 5000 cycles	[22]
SnO2@RGO	Sol-gel-thermal reduction	2 mV s^{-1}	PVA/KOH	229.1	80% after 1000cycles	[47]

SnO$_2$ nanosheets @Carbon cloth	Chemical	1 A g^{-1}	0.5 M LiNO$_3$	247	76.9% after 10 000 cycles	[14]
SnO$_2$@rGO	Dynamic self assembly	5 mV s^{-1}	2 M KOH	257	90% after 1000 cycles	[48]
SnO$_X$@CNF	Electrospinning	1 mV s^{-1}	1 M KOH	289	88 % after 5000 cycles	[15]
SnO$_2$@Graphene	solvothermal	10 mV s^{-1}	1 M H$_2$SO$_4$	363.3	-	[49]
SnO$_2$ @Graphene	hydrothermal	4.5 A g^{-1}	1M H$_2$SO$_4$	396	92.6% after 10000cycles	[25]
SnO$_2$@C microspheres	Chemical	1 A g^{-1}	1 M KOH	420	91 % after 2000 cycles	[50]
SnO$_2$ @Graphene	Chemical	1 mV s^{-1}	6 M KOH	818.6	95.1% after 1000cycles	[51]
SnO$_2$@C beads	Chemical	1 A g^{-1}	1 M KOH	432	95.5 % after 2000 cycles	Our work

Charge storage mechanism in SnO$_2$@C composite materials can be evaluated by the formula

$$i = av^b \tag{3}$$

a, b were the adjustable parameters. These parameters were obtained by the linear plot between the log *i* vs log *v* as shown in Fig. 6a. When b =1, it is capacitive and b = 0.5 typical diffusion-controlled charge storage [52]. SnO$_2$@C composite electrodes show the b value in the range between the 0.38-0.49 at a scan rate of 5 to 100 mV s^{-1}, which confirms the charge storage mechanism in SnO$_2$@C composite electrodes corresponds to diffusion-controlled charge storage phenomenon. (shown in Table.3). Pseudocapacitive charge storage is mainly attributed from the surface reactions occurs in the SnO$_2$@C composite.

Table 3. b value calculated from the slopes of log i vs log v presented in Fig. 6a. R^2, the goodness of linear fit is also presented for clarity

Voltage	R^2	b- value
0	0.99808	0.47436
-0.1	0.9948	0.49856
-0.2	0.99576	0.49009
-0.3	0.99499	0.45706
-0.4	0.99555	0.38747

Cycle stability of the electrode at 2 A g^{-1} charge-discharge (Fig. 6b) shows the electrodes shows 95.5 % capacity retention at the end of 2000 cycles. The small capacitance fade in the charge-discharge cycles is due to the degradation of the material such as dispersion or dissolved in the electrolyte, irreversible surface changes, etc. Charge-discharge curves before and after 2000 cycles is shown in Supplementary Fig.S8. The material shows very stable electrochemical performance for 2000 cycles with little decay. During 2000 cycles the IR drop increases a little in relation to the 1st cycle. The enhanced cyclic stability is due to restricted crystal growth of SnO_2 as well as diffusion kinetics because of the mesoporous structure of carbon and SnO_2 exist in the $SnO_2@C$ composite. During cycling, it absorbs more amount of electrolyte and enhances more charge storage property of the composite.

The Ragone plot of the composite electrode (w.r.t. various current densities) is evaluated by using the following equations from charge-discharge curves is shown in Fig. 6c

$$E = \frac{C(\Delta V)^2}{7.2} \qquad (4)$$

$$P = \frac{E \times 3600}{t} \qquad\qquad (5)$$

Where E, P, C, ΔV and Δt represents energy density (Wh kg^{-1}), power density (W kg^{-1}), specific capacitance (F g^{-1}), electrochemical potential window in V and time (seconds) respectively.

SnO$_2$@C composite electrode delivers an energy density of 29.4 W h kg^{-1} at a power density of 417 W kg^{-1}. When power density reaches 3292 W kg^{-1} the energy density is 19 W h kg^{-1} at 10 A g^{-1} current density. The energy and power densities of SnO$_2$@C of the present work is compared with the previous literature reports is shown in Supplementary Table. S3. Improved electrochemical performance of SnO$_2$@C composite electrode is attributed due to SnO$_2$ which are distributed on to the carbon matrix and prevent the agglomeration of the particles and enhances the double-layer capacitance. Good interfacial contact between the SnO$_2$ and carbon particles, accessibility of electrolyte ions into the pores, spherical morphology of carbons having the mesopores and micropores which are favourable for more charge storage and facilitate the ion transport and thereby shows improved electrochemical performance.

Nyquist plots of the SnO$_2$@C composite electrodes before and after 2000 cycles are shown in Fig. 6d. The solution resistance (equivalent series resistance (ESR)) which consists of the ionic resistance of the electrolyte, intrinsic resistance of active material, and contact resistance of the active material/current collector found to be 0.14 ohm cm^2, 0.88 ohm cm^2 before and after cycling, respectively. Low ESR value shows the good conductivity of the electrode during cycling. The little change in charge transfer resistance (R$_{ct}$) before and after cycling, 5.64 and 6.63 ohm cm^2, respectively further supports good stability and improved electrochemical performances.

The overall enhanced electrochemical performance is due to the formation of the mesoporous structure of SnO_2 and carbon existed in the $SnO_2@C$ beads. Ease of access for the more electrolyte ions towards the electrode can be guaranteed by the unique mesoporous structure, electrolyte ions (K^+ and OH^-) are more utilized in the spherical $SnO_2@C$ beads. The improved specific capacitance is attributed to the pseudocapacitive behaviour of SnO_2 and EDLC behaviour of C in 1 M aqueous KOH electrolyte solution.

3.3 Teardown analysis

Fig. 7a and 7b show the FESEM images of $SnO_2@C$ composite before and after 2000 cycles, respectively. The morphology of $SnO_2@C$ remains unchanged indicating good stability of the electrode for 2000 cycles. This is due to the restricted crystal growth of SnO_2 in the porous carbon matrix. There is little change in the morphology after cycling, due to K^+ ion adsorbed/desorbed on the surface of the electrode. This is further supported by EDAX analysis which shows about 7.7 % K^+ ions in the matrix (Table.4). The increase in oxygen wt % (Table .4) after cycling is due to adsorption-desorption of OH^- in the matrix.

Table 4. Elemental compositions of $SnO_2@C$ composite before and after cycling from EDS.

Element	Before cycling (wt.%)	After cycling (wt.%)
C	41.3	35.30
O	8.7	10.7
Sn	50	46.3
K	0	7.7

4. Conclusion

In this work, the porous SnO_2@C composite is synthesized by a simple impregnation method. The SnO_2 nanoparticles are uniformly distributed into the pores of the polymer beads resulting in the mesoporous SnO_2@C composite. SnO_2@C composite electrode delivers superior specific capacitance of 432 F g^{-1} at 1 A g^{-1} current density in 1M KOH electrolyte. The improved specific capacitance is attributed to the pseudocapacitive behaviour of SnO_2 and EDLC behaviour of carbon. The mesoporous structure of carbon and SnO_2 provides continuous electron path and improves the electrochemical performance. The bimodal distribution of pores in the carbon matrix delivered a double porous electrode structure and allows full accessibility of electrolyte ions to SnO_2, enhancing the overall electrochemical performance. The SnO_2@C composite displays 95.5% capacitance retention for 2000 cycles. It also delivers an energy density of 29.4 Wh kg^{-1} and power density of 417 W kg^{-1} at 1A g^{-1} current density.

Contribution of Individual Authors

1. Malothu Usha Rani: Methodology, synthesis and structural characterization of materials, data analysis, validation, writing- original draft, writing- review and editing

2 Vangapally Naresh: Electrochemical characterization, data analysis, validation, writing- original draft, writing- review and editing

3. Devarakonda Damodar: Structural characterization of materials, data analysis, validation,

4. Sadananda Muduli: Electrochemical characterization, data analysis, validation,

5. Surendra Kumar Martha: Resources, conceptualization, methodology supervision, validation, writing- original draft, writing- review and editing

6. Atul Suresh Deshpande: Resources conceptualization, methodology, supervision, validation, writing- original draft, writing- review and editing

Declaration of interests

The authors declare no conflict of interest.

Acknowledgement

References

[1] L. Hao, X. Li, L. Zhi, Carbonaceous electrode materials for supercapacitors, Adv. Mater. Weinheim. 25 (2013) 3899–3904. https://doi.org/10.1002/adma.201301204.

[2] K. Wang, N. Zhao, S. Lei, R. Yan, X. Tian, J. Wang, Y. Song, D. Xu, Q. Guo, L. Liu, Promising biomass-based activated carbons derived from willow catkins for high performance supercapacitors, Electrochim. Acta. 166 (2015) 1–11. https://doi.org/10.1016/j.electacta.2015.03.048.

[3] L.-F. Chen, X.-D. Zhang, H.-W. Liang, M. Kong, Q.-F. Guan, P. Chen, Z.-Y. Wu, S.-H. Yu, Synthesis of Nitrogen-Doped Porous Carbon Nanofibers as an Efficient Electrode Material for Supercapacitors, ACS Nano. 6 (2012) 7092–7102. https://doi.org/10.1021/nn302147s.

[4] C. Liu, Z. Yu, D. Neff, A. Zhamu, B.Z. Jang, Graphene-Based Supercapacitor with an Ultrahigh Energy Density, Nano Lett. 10 (2010) 4863–4868. https://doi.org/10.1021/nl102661q.

[5] Q.-L. Chen, K.-H. Xue, W. Shen, F.-F. Tao, S.-Y. Yin, W. Xu, Fabrication and electrochemical properties of carbon nanotube array electrode for supercapacitors, Electrochim. Acta. 49 (2004) 4157–4161. https://doi.org/10.1016/j.electacta.2004.04.010.

[6] J. Yang, H. Wu, M. Zhu, W. Ren, Y. Lin, H. Chen, F. Pan, Optimized mesopores enabling enhanced rate performance in novel ultrahigh surface area meso-/microporous carbon for supercapacitors, Nano Energy. 33 (2017) 453–461. https://doi.org/10.1016/j.nanoen.2017.02.007.

[7] M. Yoshimune, T. Yamamoto, M. Nakaiwa, K. Haraya, Preparation of highly mesoporous carbon membranes via a sol–gel process using resorcinol and formaldehyde, Carbon. 46 (2008) 1031–1036. https://doi.org/10.1016/j.carbon.2008.03.007.

[8] G. Xin, Y. Wang, S. Jia, P. Tian, S. Zhou, J. Zang, Synthesis of nitrogen-doped mesoporous carbon from polyaniline with an F127 template for high-performance supercapacitors, Appl. Surf. Sci. 422 (2017). https://doi.org/10.1016/j.apsusc.2017.06.084.

[9] D. Wang, Z. Geng, B. Li, C. Zhang, High performance electrode materials for electric double-layer capacitors based on biomass-derived activated carbons, Electrochim. Acta. 173 (2015) 377–384. https://doi.org/10.1016/j.electacta.2015.05.080.

[10] K. Liang, W. Wang, Y. Yu, L. Liu, H. Lv, Y. Zhang, A. Chen, Synthesis of nitrogen-doped mesoporous carbon for high-performance supercapacitors, New J. Chem. 43 (2019) 2776–2782. https://doi.org/10.1039/C8NJ05938A.

[11] V. Malgras, J. Tang, J. Wang, J. Kim, N. Torad, S. Dutta, K. Ariga, M. Hossain, Y. Yamauchi, K. Wu, Fabrication of Nanoporous Carbon Materials with Hard- and Soft-Templating Approaches: A Review, J. Nanosci. Nanotechnol. 19 (2019) 3673–3685. https://doi.org/10.1166/jnn.2019.16745.

[12] Y.S. Yun, S.Y. Cho, J. Shim, B.H. Kim, S.-J. Chang, S.J. Baek, Y.S. Huh, Y. Tak, Y.W. Park, S. Park, H.-J. Jin, Microporous Carbon Nanoplates from Regenerated Silk Proteins for Supercapacitors, Adv. Mater. 25 (2013) 1993–1998. https://doi.org/10.1002/adma.201204692

[13] M.Y. Ho, P.S. Khiew, D. Isa, T.K. Tan, W.S. Chiu, C.H. Chia, A review of metal oxide composite electrode materials for electrochemical capacitors, Nano. 09 (2014) 1430002. https://doi.org/10.1142/S1793292014300023

[14] Zhang, Z. Hu, Y. Liang, Y. Yang, N. An, Z. Li, H. Wu, Growth of 3D SnO_2 nanosheets on carbon cloth as a binder-free electrode for supercapacitors, J. Mater. Chem. A. 3 (2015) 15057–15067. https://doi.org/10.1039/C5TA02479J

[15] E. Samuel, B. Joshi, H.S. Jo, Y.I. Kim, M.T. Swihart, J.M. Yun, K.H. Kim, S.S. Yoon, Flexible and freestanding core-shell SnOx/carbon nanofiber mats for high-performance supercapacitors, J. Alloys Compd. 728 (2017) 1362–1371. https://doi.org/10.1016/j.jallcom.2017.09.103.

[16] P. Liu, B. Tang, J. Zhao, J. Feng, J. Xu, Ordered mesoporous carbon/SnO_2 composites as the electrode material for supercapacitors, J. Wuhan Univ. Technol.-Mat. Sci. Edit. 26 (2011) 407–411. https://doi.org/10.1007/s11595-011-0239-8.

[17] J. Li, X. Zhang, J. Guo, R. Peng, R. Xie, Y. Huang, Y. Qi, Facile surfactant- and template-free synthesis and electrochemical properties of SnO_2/graphene composites, J. Alloys. Compd. 674 (2016) 44–50. https://doi.org/10.1016/j.jallcom.2016.02.212.

[18] R.B. Rakhi, W. Chen, D. Cha, H.N. Alshareef, High performance supercapacitors using metal oxide anchored graphene nanosheet electrodes, J. Mater. Chem. 21 (2011) 16197–16204. https://doi.org/10.1039/C1JM12963E.

[19] Y. Luan, G. Nie, X. Zhao, N. Qiao, X. Liu, H. Wang, X. Zhang, Y. Chen, Y.-Z. Long, the integration of SnO_2 dots and porous carbon nanofibers for flexible supercapacitors, Electrochim. Acta. 308 (2019) 121–130. https://doi.org/10.1016/j.electacta.2019.03.204.

[20] Z. Li, T. Chang, G. Yun, J. Guo, B. Yang, 2D tin dioxide nanoplatelets decorated graphene with enhanced performance supercapacitor, J.Alloys.Compd. 586 (2014) 353–359. https://doi.org/10.1016/j.jallcom.2013.10.037.

[21]   J. Mu, B. Chen, Z. Guo, M. Zhang, Z. Zhang, C. Shao, Y. Liu, Tin oxide (SnO2) nanoparticles/electrospun carbon nanofibers (CNFs) heterostructures: controlled fabrication and high capacitive behavior, J Colloid Interface Sci. 356 (2011) 706–712. https://doi.org/10.1016/j.jcis.2011.01.032.

[22] X. Hong, S. Li, R. Wang, J. Fu, Hierarchical SnO_2 nanoclusters wrapped functionalized carbonized cotton cloth for symmetrical supercapacitor, J. Alloys. Compd. 775 (2019) 15–21. https://doi.org/10.1016/j.jallcom.2018.10.099.

[23]   Z.J. Li, T.X. Chang, G.Q. Yun, Y. Jia, Coating single walled carbon nanotube with SnO_2 and its electrochemical properties, Powder Technol. 224 (2012) 306–310. https://doi.org/10.1016/j.powtec.2012.03.012.

[24]   C.-T. Hsieh, W.-Y. Lee, C.-E. Lee, H. Teng, Electrochemical Capacitors Fabricated with Tin Oxide/Graphene Oxide Nanocomposites, J. Phys. Chem. C. 118 (2014) 15146–15153. https://doi.org/10.1021/jp502958w.

[25] Y. Haldorai, Y.S. Huh, Y.-K. Han, Surfactant-assisted hydrothermal synthesis of flower-like tin oxide/graphene composites for high-performance supercapacitors, New J. Chem. 39 (2015) 8505–8512. https://doi.org/10.1039/C5NJ01442E.

[26] A.S. Deshpande, M. Niederberger, Synthesis of mesoporous ceria zirconia beads, Microporous Mesoporous Mater. 101 (2007) 413–418. https://doi.org/10.1016/j.micromeso.2006.11.036

[27] A. Dhanabalan, R. Agrawal, C. Chen, C. Wang, Fabrication and Characterization of SnO_2/Graphene Composites as High Capacity Anodes for Li-Ion Batteries, Nanomaterials. 3 (2013) 606–614. https://doi.org/10.3390/nano3040606.

[28] X. Zhou, W. Liu, X. Yu, Y. Liu, Y. Fang, S. Klankowski, Y. Yang, J.E. Brown, J. Li, Tin Dioxide@Carbon Core–Shell Nanoarchitectures Anchored on Wrinkled Graphene

for Ultrafast and Stable Lithium Storage, ACS Appl. Mater. Interfaces. 6 (2014) 7434–7443. https://doi.org/10.1021/am5007194.

[29] P. Gurunathan, P. Ette, K. Ramesha, Synthesis of Hierarchically Porous SnO2 Microspheres and Performance Evaluation as Li-Ion Battery Anode by Using Different Binders, ACS Appl. Mater. Interfaces. 6 (2014). https://doi.org/10.1021/am502852x.

[30] P. Rambabu, S.K. Srivastava, P. Das, G.R. Turpu, rGO- SnO$_2$ Composites for Supercapacitor Applications, IOP Conference Series: Materials Science and Engineering. 149 (2016) 012169. https://doi.org/10.1088/1757-899X/149/1/012169.

[31] I.I. Misnon, N.K.M. Zain, T.S. Lei, B.L. Vijayan, R. Jose, Activated carbon with graphitic content from stinky bean seedpod biowaste as supercapacitive electrode material, Ionics. (2020). https://doi.org/10.1007/s11581-020-03565-x.

[32] B. Li, F. Dai, Q. Xiao, L. Yang, J. Shen, C. Zhang, M. Cai, Activated Carbon from Biomass Transfer for High-Energy Density Lithium-Ion Supercapacitors, Adv. Energy Mater. 6 (2016) 1600802. https://doi.org/10.1002/aenm.201600802.

[33] K. Wang, N. Zhao, S. Lei, R. Yan, X. Tian, J. Wang, Y. Song, D. Xu, Q. Guo, L. Liu, Promising biomass-based activated carbons derived from willow catkins for high performance supercapacitors, Electrochim Acta. 166 (2015) 1–11. https://doi.org/10.1016/j.electacta.2015.03.048.

[34] K. Jurkiewicz, M. Pawlyta, D. Zygadło, D. Chrobak, S. Duber, R. Wrzalik, A. Ratuszna, A. Burian, Evolution of glassy carbon under heat treatment: correlation structure–mechanical properties, J. Mater. Sci. 53 (2018). https://doi.org/10.1007/s10853-017-1753-7.

[35] F. Lufrano, P. Staiti, Mesoporous Carbon Materials as Electrodes for Electrochemical Supercapacitors, Int.J. Electrochem. 5 (2010) 903–916.

[36] J. Guo, P. Li, L. Chai, Y. Su, J. Diao, X. Guo, Silica template-assisted synthesis of SnO_2@porous carbon composites as anode materials with excellent rate capability and cycling stability for lithium-ion batteries, RSC Adv. 7 (2017) 30070–30079. https://doi.org/10.1039/C7RA03594B

[37] M.F.N. Taufique, A. Bhaumik, A. Haque, P. Karnati, Reduced Graphene Oxide Thin Films with Very Large Charge Carrier Mobility Using Pulsed Laser Deposition, J Material Sci Eng. 06 (2017). https://doi.org/10.4172/2169-0022.1000364.

[38] L. Tang, X. Li, R. Ji, K.S. Teng, G. Tai, J. Ye, C. Wei, S.P. Lau, Bottom-up synthesis of large-scale graphene oxide nanosheets, J. Mater. Chem. 22 (2012) 5676–5683. https://doi.org/10.1039/C2JM15944A.

[39] Q.B. Bui, D.M. Nguyen, T.M.L. Nguyen, L.K. Kwac, H.G. Kim, S.C. Ko, H. Jeong, Free-standing three dimensional graphene incorporated with gold nanoparticles as novel binder-free electrochemical sensor for enhanced glucose detection, J.Electrochem. Sci. Technol. 9 (2018) 229–237. https://doi.org/10.5229/JECST.2018.9.3.229

[40] L.-Q. Mai, A. Minhas-Khan, X. Tian, K.M. Hercule, Y.-L. Zhao, X. Lin, X. Xu, Synergistic interaction between redox-active electrolyte and binder-free functionalized carbon for ultrahigh supercapacitor performance, Nature Communications. 4 (2013) 2923. https://doi.org/10.1038/ncomms3923.

[41] R.K. Selvan, I. Perelshtein, N. Perkas, A. Gedanken, Synthesis of Hexagonal-Shaped SnO_2 Nanocrystals and SnO_2@C Nanocomposites for Electrochemical Redox

Supercapacitors, J. Phys. Chem. C. 112 (2008) 1825–1830. https://doi.org/10.1021/jp076995q.

[42] S.-W. Hwang, S.-H. Hyun, Synthesis and characterization of tin oxide/carbon aerogel composite electrodes for electrochemical supercapacitors, J Power Sources. 172 (2007) 451–459. https://doi.org/10.1016/j.jpowsour.2007.07.061.

[43] J. Ge, Y. Qu, L. Cao, F. Wang, L. Dou, J. Yu, B. Ding, Polybenzoxazine-based highly porous carbon nanofibrous membranes hybridized by tin oxide nanoclusters: durable mechanical elasticity and capacitive performance, J. Mater. Chem. A. 4 (2016) 7795–7804. https://doi.org/10.1039/C6TA00762G.

[44] V. Vinoth, J.J. Wu, A.M. Asiri, T. Lana-Villarreal, P. Bonete, S. Anandan, SnO_2-decorated multiwalled carbon nanotubes and Vulcan carbon through a sonochemical approach for supercapacitor applications, Ultrason. Sonochem. 29 (2016) 205–212. https://doi.org/10.1016/j.ultsonch.2015.09.013.

[45] V. Naresh, S.K. Martha, Carbon Coated SnO_2 as a Negative Electrode Additive for High Performance Lead Acid Batteries and Supercapacitors, J. Electrochem. Soc. 166 (2019) A551–A558. https://doi.org/10.1149/2.0291904jes.

[46] C.-M. Chen, Q. Zhang, J.-Q. Huang, W. Zhang, X.-C. Zhao, C.-H. Huang, F. Wei, Y.-G. Yang, M.-Z. Wang, D.S. Su, Chemically derived graphene–metal oxide hybrids as electrodes for electrochemical energy storage: pre-graphenization or post-graphenization?, J. Mater. Chem. 22 (2012) 13947–13955. https://doi.org/10.1039/C2JM16042K.

[47] R. Hu, J. Zhao, J. Zheng, Synthesis of SnO_2/rGO hybrid materials by sol-gel/thermal reduction method and its application in electrochemical capacitors, Mater.Lett. 197 (2017) 59–62. https://doi.org/10.1016/j.matlet.2017.03.082

[48] M. Chen, H. Wang, L. Li, Z. Zhang, C. Wang, Y. Liu, W. Wang, J. Gao, Novel and Facile Method, Dynamic Self-Assemble, To Prepare SnO_2/rGO Droplet Aerogel with Complex Morphologies and Their Application in Supercapacitors, ACS Appl. Mater. Interfaces. 6 (2014) 14327–14337. https://doi.org/10.1021/am5036169.

[49] S.P. Lim, N.M. Huang, H.N. Lim, Solvothermal synthesis of SnO_2/graphene nanocomposites for supercapacitor application, Ceram.Int. 39 (2013) 6647–6655. https://doi.org/10.1016/j.ceramint.2013.01.102.

[50] C. He, Y. Xiao, H. Dong, Y. Liu, M. Zheng, K. Xiao, X. Liu, H. Zhang, B. Lei, Mosaic-Structured SnO_2@C Porous Microspheres for High-Performance Supercapacitor Electrode Materials, Electrochim. Acta. 142 (2014) 157–166. https://doi.org/10.1016/j.electacta.2014.07.077

[51] V. Velmurugan, U. Srinivasarao, R. Ramachandran, M. Saranya, A.N. Grace, Synthesis of tin oxide/graphene (SnO_2/G) nanocomposite and its electrochemical properties for supercapacitor applications, Mater. Res. Bull. 84 (2016) 145–151. https://doi.org/10.1016/j.materresbull.2016.07.015.

[52] Y. Wang, Y. Song, Y. Xia, Electrochemical capacitors: mechanism, materials, systems, characterization and applications, Chem. Soc. Rev. 45 (2016) 5925–5950. https://doi.org/10.1039/C5CS00580A.

[53] S. Ren, Y. Yang, M. Xu, H. Cai, C. Hao, X. Wang, Hollow SnO_2 microspheres and their carbon-coated composites for supercapacitors, Colloids Surf. 444 (2014) 26–32. https://doi.org/10.1016/j.colsurfa.2013.12.028.

[54] N.-L. Wu, Nanocrystalline oxide supercapacitors, Mater Chem. Phys. 75 (2002) 6–11. https://doi.org/10.1016/S0254-0584(02)00022-6.

[55] V. Bonu, B. Gupta, S. Chandra, A. Das, S. Dhara, A.K. Tyagi, Electrochemical supercapacitor performance of SnO_2 quantum dots, Electrochim Acta. 203 (2016) 230–237. https://doi.org/10.1016/j.electacta.2016.03.153.

[56] K. Manikandan, S. Dhanuskodi, N. Maheswari, G. Muralidharan, SnO_2 nanoparticles for supercapacitor application, AIP Conference Proceedings. 1731 (2016) 050048. https://doi.org/10.1063/1.4947702.
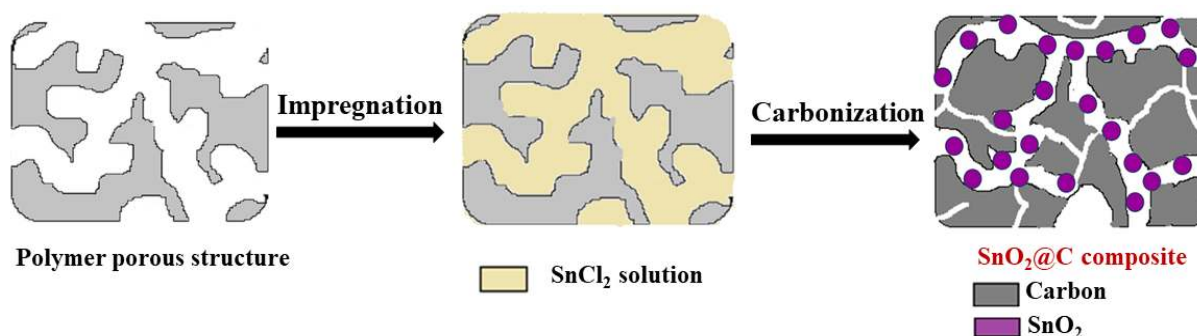
Scheme.1. Schematic representation of the synthesis of SnO_2@C composite obtained from porous polymer beads
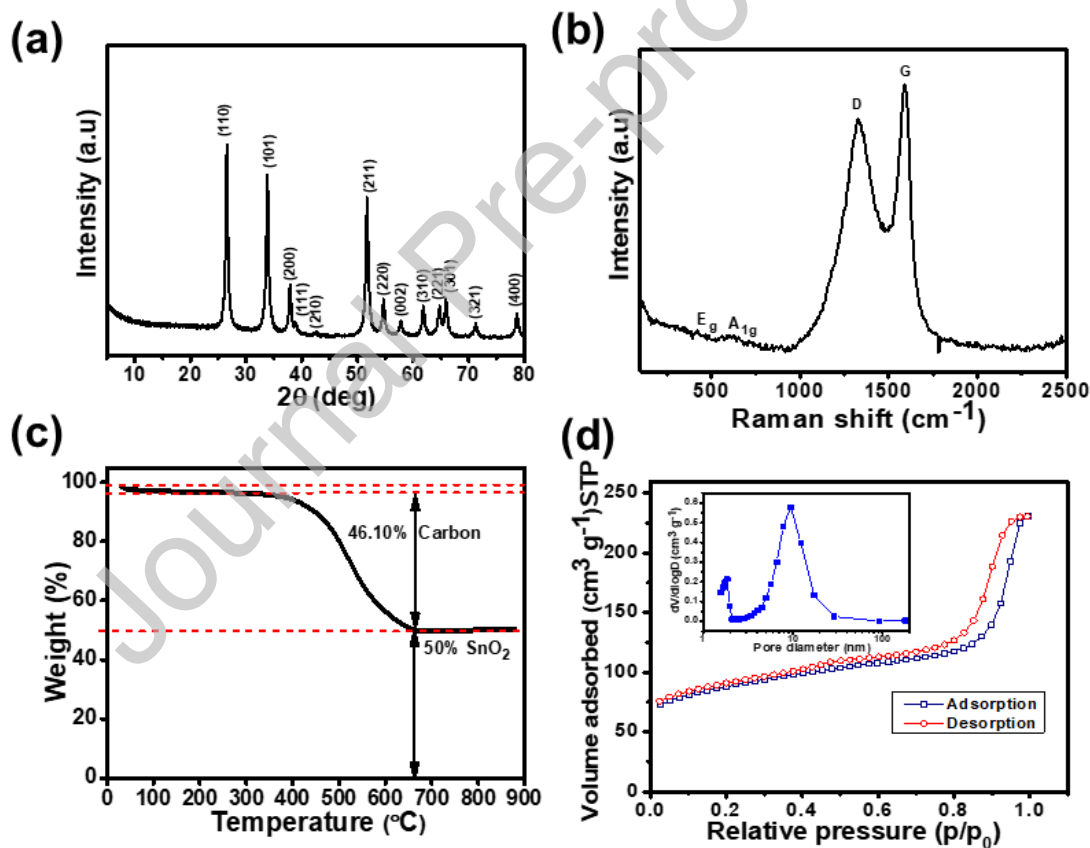
Fig. 1. (a) XRD of SnO_2@C composite, (b) Raman spectrum of SnO_2@C composite, (c) TGA of SnO_2@C composite, (d) BET Isotherm and the inset shows the pore size distribution of SnO_2@C composite.
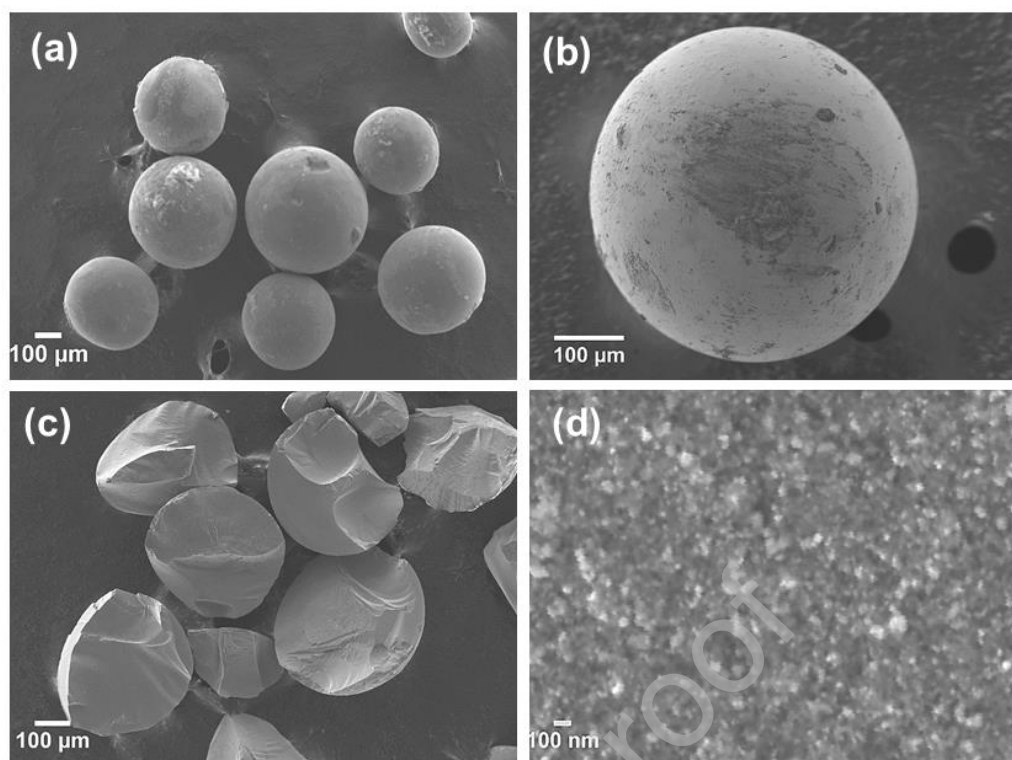
Fig. 2. (a) and (b) FESEM Images of $SnO_2@C$ beads at different magnifications, (c) FESEM Image of broken $SnO_2@C$ beads and (d) High magnification image of the broken part of $SnO_2@C$ bead
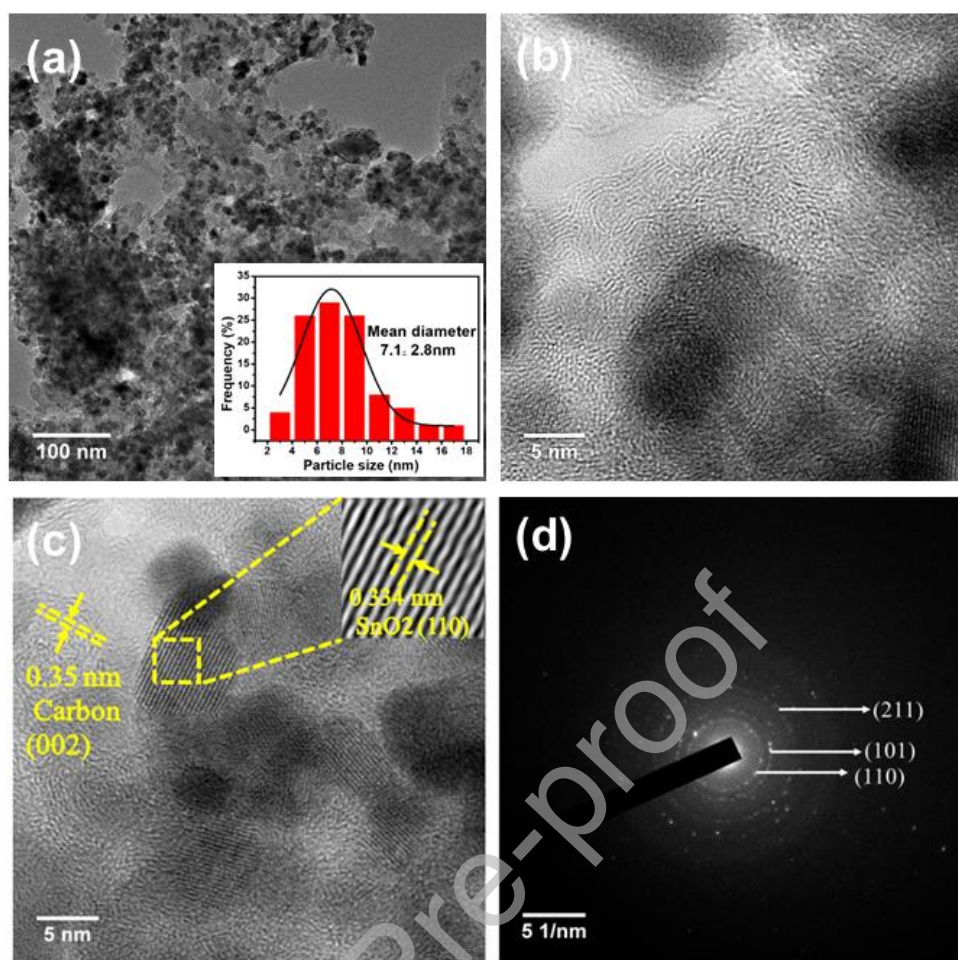
Fig. 3. (a) Low-magnification TEM image of SnO_2@C composite and inset shows particle size distribution of SnO_2, (b) TEM image of SnO_2@C showing porosity (c) High magnification TEM image of SnO_2@C showing the lattice fringes of carbon and SnO_2(inset), and (d) SAED pattern of SnO_2.
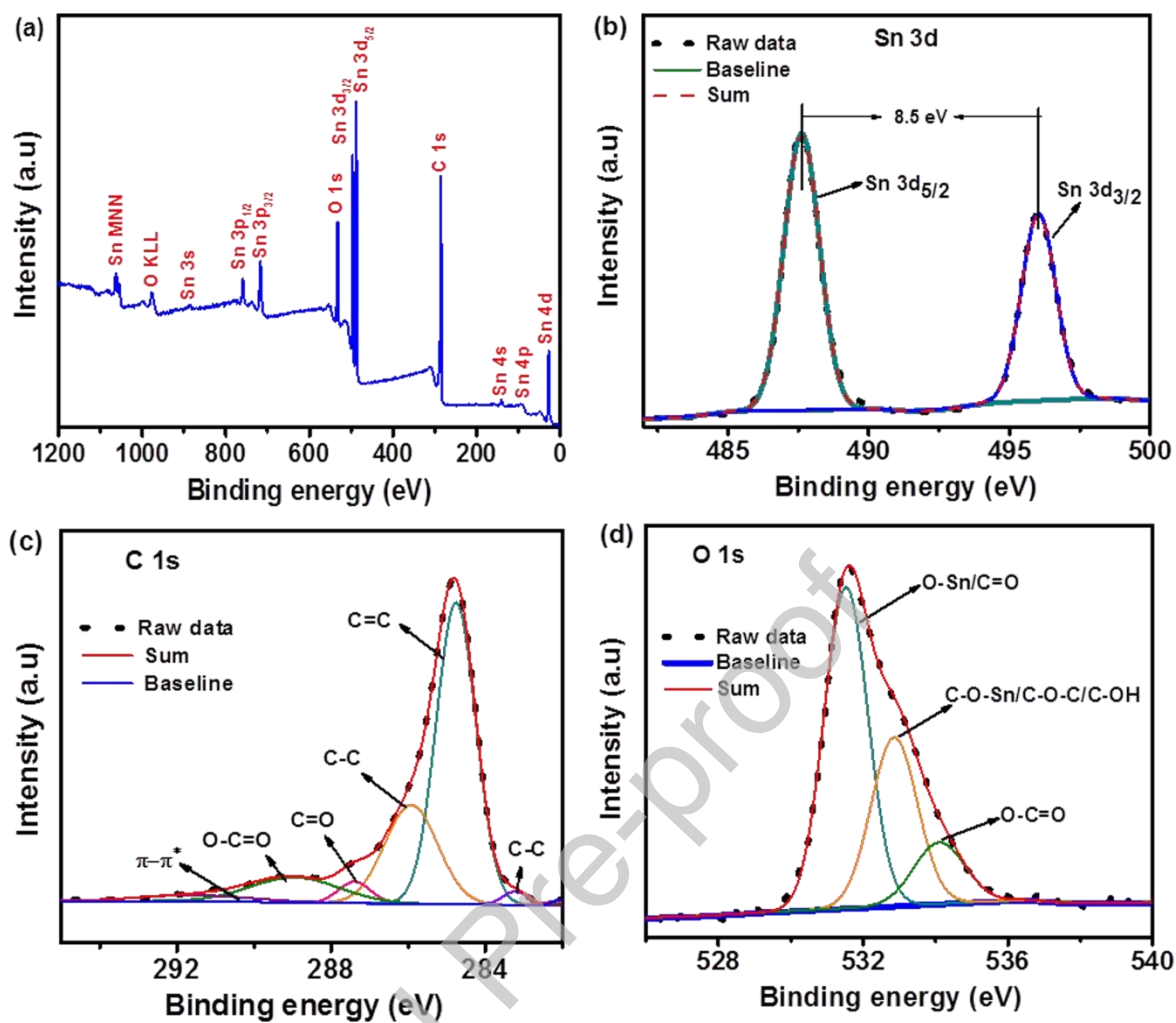
Fig. 4. (a) XPS survey spectrum of $SnO_2@C$ composite, (b) XPS spectrum of Sn 3d of $SnO_2@C$ composite, (c) C 1s spectrum of $SnO_2@C$ composite, and (d) O 1s spectrum of $SnO_2@C$ composite.
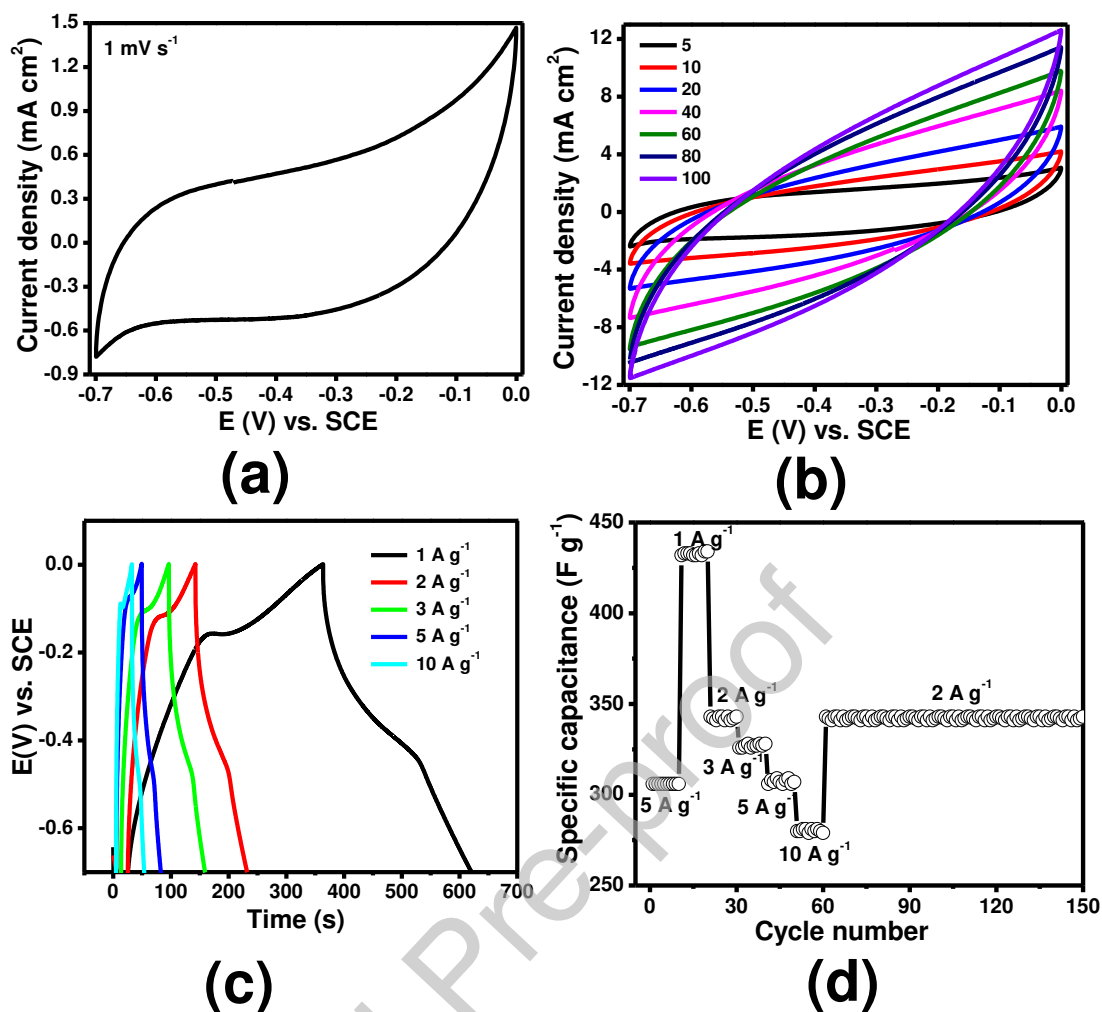
Fig. 5. CVs at (a) High, (b) Low scan rates, (c) Galvanostatic charge-discharge curves of $SnO_2@C$ at different current densities, (d) Rate capability performance of $SnO_2@C$ composite in 1 M KOH solution.
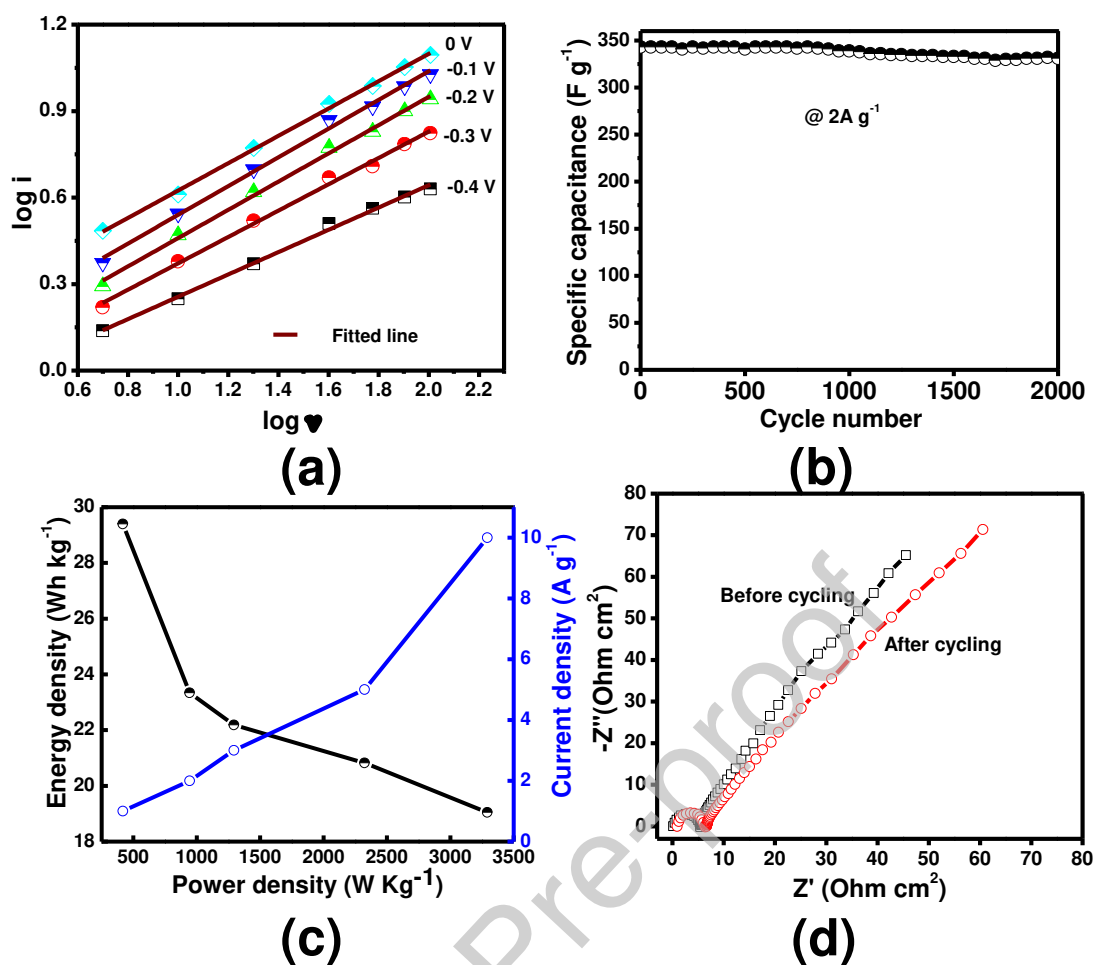
Fig. 6. (a) Linear fit of log i vs log v obtained from the CV curves from Fig. 5b at different scan rates, (b) Cycling performance of $SnO_2@C$ beads at a current density of 2 A g^{-1}, (c) energy density vs. power density, (d) Nyquist plots of $SnO_2@C$ beads in the frequency range between 1 MHz and 10 mHz before and after 2000 cycles.
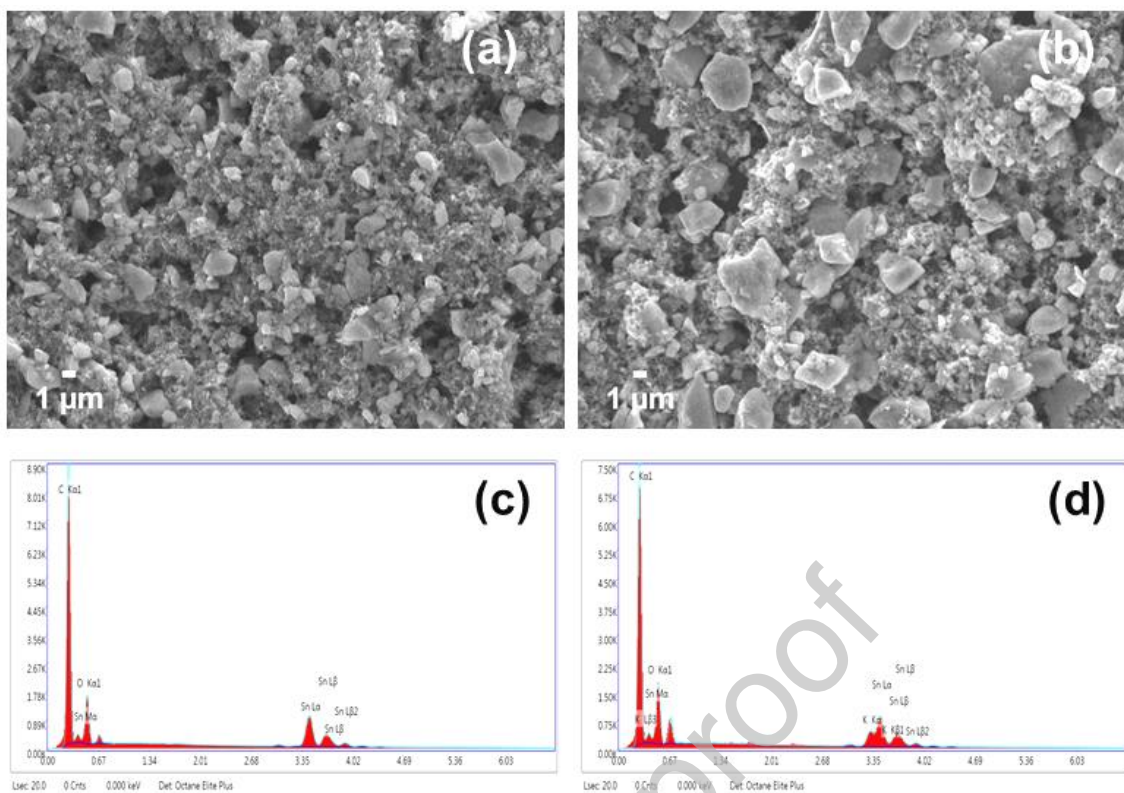
Fig. 7. FESEM image shows the teardown analysis of SnO_2@C composite (a) before cycling and (b) after 2000 cycles, EDS showing the elemental composition of SnO_2@C composite (c) before cycling and (d) after 2000 cycles.